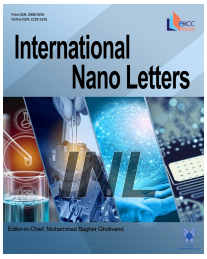

Volume 14, Issue 3, 142411 (1-15)

International Nano Letters (INL)

https://doi.org/10.57647/inl.2024.1403.11

Selenium Chitosan and Selenium Carboxymethyl Chitosan Nanoparticles Combined with Curcumin Chitosan Nanoparticles to Enhance Antibacterial and Antiviral Activities

Zahra Tavakoli[1], Reza Aalizadeh[2], Khosro Khajeh[3], Bijan Ranjbar[1,4,*]

[1]*Department of Nanobiotechnology, Faculty of Biological Sciences, Tarbiat Modares University, Tehran, Iran.*
[2]*Department of Nanobiotechnology and Biomimetics School of Life Science Engineering College of Interdisciplinary Science and Technology, University of Tehran, Tehran, Iran.*
[3]*Department of Biochemistry, Faculty of Biological Science, Tarbiat Modares University, Tehran, Iran.*
[4]*Department of Biophysics, Faculty of Biological Sciences, Tarbiat Modares University, Tehran, Iran.*

[*]**Corresponding author:** ranjbarb@modares.ac.ir

Original Research

Abstract:

The use of nanoparticles is a promising strategy for combating pathogenic microorganisms. This study introduces a novel hybrid nanosystem combining selenium nanoparticles (Se NPs) with curcumin-loaded chitosan nanoparticles (Cur-CS NPs) to enhance antimicrobial efficacy. The results indicate that increasing the rotation speed to 1500 rpm, the potassium iodide and ascorbic acid concentrations to 40 mM and 70 mM, respectively, leads to the production of smaller Se NPs. Furthermore, Cur-CS NPs, prepared via ionotropic gelation, exhibited a pH-dependent release profile. Two hybrid systems were developed, one combining Se-chitosan NPs (Se-CS, 73 nm) with Cur-CS NPs, and another combining Se-carboxymethyl chitosan NPs (Se-CMCS, 80 nm) with Cur-CS NPs. Both combinations demonstrated remarkable broad-spectrum antibacterial activity, with similar minimum inhibitory concentrations (0.570–1.251 µg/mL) and minimum bactericidal concentrations against *E. coli* (1.251 µg/mL) and *S. aureus* (9.251 µg/mL). Furthermore, Se-CS@Cur-CS NPs demonstrated potent antiviral activity, exhibiting a two-fold higher efficacy in inhibiting SARS-CoV-2 compared to Se-CMCS@Cur-CS NPs. All systems maintained excellent biocompatibility, showing no cytotoxicity to Vero cells at concentrations up to 110 µg/mL. These findings suggest a synergistic effect between stabilized selenium nanoparticles and Cur-CS NPs, yielding a multifunctional platform with dual antibacterial and antiviral capabilities.

Keywords:

Selenium; Nanoparticle; Curcumin; Chitosan; Carboxymethyl Chitosan

Cite this article: Tavakoli, Z., Aalizadeh, R., Khajeh, K., Ranjbar, B. Selenium Chitosan and Selenium Carboxymethyl Chitosan Nanoparticles Combined with Curcumin Chitosan Nanoparticles to Enhance Antibacterial and Antiviral Activities. *Int. Nano Lett.* **14**(3), 142411 (2024).

1. Introduction

The advent of antibiotics and other antimicrobial agents has significantly advanced the treatment of infectious diseases. However, resistant and emerging microorganisms have caused serious problems with contagious diseases. For example, the first prevalence of Severe Acute Respiratory Syndrome Coronavirus-2 (SARS-CoV-2), the causative agent of Coronavirus Disease 2019 (COVID-19), was reported in December 2019 [1, 2]. Conventional drug delivery systems suffer from significant shortcomings in selective targeting, drug dissolution, cellular uptake, and bioavailability, often resulting in adverse effects. Consequently, novel systems must be developed to improve clinical outcomes [3, 4]. The controllable size and surface chemistry of nanomaterials facilitate targeted drug design and improve drug circulation and blood retention times [5]. Due to their nanoscale dimensions (10-100 nm), nanomaterials can efficiently cross the cell membrane via phagocytosis and enter host cells through endocytosis, which minimizes the occurrence of adverse effects associated with pharmaceuticals [6–11]. Some NPs (Ag and ZnO NPs) have been shown to overcome the efflux mechanism in bacterial cells, thereby

limiting drug uptake and enabling higher doses to be administered at the infection site [12, 13]. Nanoparticle-based therapies can inhibit the effects of infection agents in various approaches, including external inactivation, blocking the receptor binding/microbial entry and inhibition of replication [14, 15]. In recent years, various classes of nanostructures, including metallic (Ag, Au), carbon-based (graphene, carbon dots, CNTs), magnetic, and metal oxide (ZnO/CuO) NPs, have been explored for biomedical applications [16–22].

The selenium-based nanoparticle is another potential candidate and has been identified as biocompatible, with antibacterial, antiviral, anti-inflammatory, and anticancer effects. Selenium (Se) is an essential trace element incorporated into selenoproteins [23, 24]. Many selenoproteins regulate the physiological redox balance and Se deficiency can increase susceptibility to respiratory infections. Despite these numerous benefits, excessive doses of Se can be toxic, and nanomaterial science focuses on mitigating Se toxicity while preserving its advantages [25, 26]. Zhang et al. reported that Se NPs can deliver a higher dose of Se to the body than other sources, such as selenium cysteine. Their findings indicate that the oral administration of Se NPs to mice results in less toxicity with a survival rate that is 5 times higher, and a lower incidence of liver failure compared to the same amount of selenocysteine [27]. Also, Zhang et al. demonstrated that different sizes of Se NPs (5-200 nm) have the same capacity to induce selenoenzymes in cultured cells and mice [28]. The most prevalent method for synthesizing Se NPs is chemical reduction. However, Se NPs are typically unstable and accumulate in a dark orange form. Various approaches have been used to stabilize Se NPs, including polymers, proteins, and polysaccharides. Among these, chitosan derivatives, due to their ability to provide smaller NPs, have demonstrated notable efficacy [29–31].

Chitosan (CS) is a non-toxic, biocompatible, and biodegradable natural macromolecule used to construct nanocarrier systems. Chitosan is obtained by deacetylating chitin in an alkaline environment. Studies have demonstrated that chitosan derivatives exhibit antimicrobial activity through two distinct mechanisms: Direct antimicrobial activity and the induction of antimicrobial immune responses [32, 33]. The biological activity of chitosan is influenced by its intrinsic properties, including molecular weight, degree of polymerization, degree of N-acetylation, positive charge, and chemical changes to the molecule. In chitosan structures, deacetylated amino groups facilitate dissolution in dilute acids at pH < 6.5 due to the protonation of amine groups (pKa ≈ 6.5) [34]. Chitosan does not dissolve at alkaline pH; thus, its solubility can be modified by adding functional groups. For instance, incorporating carboxyl groups with a pKa value of approximately 4.5 into carboxymethyl chitosan (CMCS) enhances solubility in neutral water and alkaline pH [35]. Furthermore, the modified structure can retain water and release the drug in a controlled manner. Chitosan derivatives have been demonstrated to facilitate cell growth, tissue regeneration, and wound healing. Furthermore, chitosan's moisture-absorbing properties and antimicrobial and emulsion-stabilizing effects have been utilized to produce cosmetic products [36].

Many reports have demonstrated that natural polyphenol compounds, incorporated into daily diets, can effectively mitigate the prevalence of various infections. Among the numerous natural antimicrobial agents, curcumin, a desirable phytochemical, has exhibited substantial therapeutic potential, particularly in the context of anticancer, antioxidant, and anti-inflammatory properties [37]. Research studies have substantiated that curcumin exerts a remarkable capacity to impede the onset or progression of diseases. Nevertheless, the substantial therapeutic value of curcumin is limited by its extensive degradation and lower bioavailability, consequently constraining its clinical application. Consequently, there is a growing interest in exploring novel formulation strategies, such as nanotechnology, to enhance the therapeutic efficacy of curcumin [46]. Various approaches were performed to incorporate or encapsulate curcumin into polymeric nanoparticles, liposomes, and self-assembled structures, resulting in active binding and enhanced drug uptake by microbial agents. Due to their unique properties, chitosan nanoparticles have emerged as promising nanostructures for encapsulating curcumin [47, 48]. Hence, this study selected CS over CMCS for the synthesis of Cur-CS NPs due to its simplicity, reproducibility, established protocols, and its ability to minimize variability during optimization. Native chitosan's cationic nature also facilitated better electrostatic binding with anionic curcumin, enhancing encapsulation efficiency and preliminary tests confirmed chitosan provided sufficient stability and high drug-loading performance [49, 50].

Herein, we used simplified chemical and ionotropic gelation methods to synthesize Se-CS NPs, Se-CMCS NPs and Cur-CS NPs to develop antimicrobial activities. First, we optimized the synthesis of the Se NPs with uniform size and narrow size distribution through a chemical reduction method by using sodium selenite as the precursor, ascorbic acid as a reductant, and potassium iodide as a stabilizer. Also, the Se NPs were modified using CS and CMCS to prevent aggregation. The capacity of this hybrid nanosystem composed of Se-CS@Cur-CS NPs and Se-CMCS@Cur-CS NPs for antibacterial activities against *E. coli* and *S. aureus* was evaluated by minimal inhibitory concentration (MIC), minimal bactericidal concentration (MBC) and disk diffusion methods. Finally, the synergistic antiviral activity of NPs against SARS-CoV-2 has to be determined. Ultraviolet-visible spectrophotometry (UV–Vis), dynamic light scattering (DLS), Fourier transform infrared (FTIR), X-ray diffraction (XRD), scanning electron microscopy (SEM), and transmission electron microscopy (TEM) were used to investigate the properties, functional groups, and surface morphologies of the synthesized NPs. So, given the significant antimicrobial roles of Se, curcumin, chitosan derivatives and the high probability of respiratory infections in individuals with selenium deficiency, it is recommended that Se-CS@Cur-CS NPs and Se-CMCS@Cur-CS NPs be employed in the fight against emerging pathogens. In addition, due to the presence of selenium in selenoproteins, optimizing the manufacturing process enables the production of safe, stable nanos-

tructures without toxic effects, making them suitable for biological applications. Several studies have investigated the antimicrobial effects of Se NPs and Curcumin. Table 1 summarizes recently used NPs comprising Se and chitosan derivatives with antimicrobial activity. This study examines a novel hybrid nanosystem integrating Cur-CS NPs with simultaneously stabilized Se-CS NPs and Se-CMCS NPs to provide synergistic broad-spectrum antibacterial activity. It also compares the antimicrobial impact of Se NPs in the presence of CS and CMCS stabilizing agents. In addition, this study provides a new opportunity to develop nanosystems with simultaneous antibacterial and antiviral effects, especially against emerging airborne viruses (such as SARS-CoV-2), which, to the best of our knowledge, have not been extensively explored. This work advances nanomedicine by delivering a multifunctional, biocompatible nanosystem with dual antibacterial/antiviral capabilities, which links gaps in infection control and pandemic preparedness.

2. Material and methods

2.1 Material

Sodium selenite (Na_2SeO_3), potassium iodide (KI), ascorbic acid ($C_6H_6O_6$), acetic acid ($C_2H_4O_2$) and triphenyl tetrazolium chloride (TTC) were purchased from Sigma Co. low molecular weight Chitosan (CS, 50 KDa, 85% degree of deacetylation), carboxymethylchitosan (CMCS, 80.12% degree of carboxylation), nutrient agar culture media (NA), Curcumin and sodium tripolyphosphate (TPP) were gained from Merck Co. Distilled water was also used to prepare solutions during the synthesis procedure. Fetal bovine serum (FBS) and dulbecco's modified eagle medium (DMEM) were purchased from Gibco. Vero cells were obtained from American Type Culture Collection (ATCC# CCL81).

2.2 Synthesis and optimization of Se NPs

Se NPs were synthesized using a modified chemical method [51]. For the synopsis, 10 mL aqueous solution of 20 mM Na_2SeO_3 was added to a 500 mL beaker. At the same time, 10 mL of 30 mM KI and 10 mL of 60 mM ascorbic acid solution were added dropwise into the mixture under magnetic stirring. Then, the final volume reached 300 mL using distilled water. Due to the reduction of selenium ions, immediately after adding the ascorbic acid, the color of the solution switched from colorless to yellowish orange. Also, due to reaching the smallest size, the reaction solution was stirred at 500, 1000, and 1500 rpm for 30 min at room temperature. The resulting colloid was centrifuged at 12000 rpm for 10 min, and the red precipitate was washed twice with water and ethanol. Finally, the hydrodynamic

Table 1. Recent nanoparticles comprised of Se and chitosan derivatives with antimicrobial activity.

Nanoparticles	Microbial agents	Results	Ref.
Se NPs in Chitosan Solution	*S.mutans*, *L.acidophilus*, and *C.albicans*.	MIC values: The concentration of 0.068 mg/mL for *S. mutans*, 0.137 mg/mL for *L. acidophilus* and 0.274 mg/mL for *C. albicans*. MBC values: The complete killing of *S. mutans*, *L. acidophilus*, and *C. albicans* at the concentration of 0.274 mg/mL of Cts-SeNPs after one, two, and six hours.	[38]
BSA-coated Se NPs	*S.enterica*, *L. Monocytogens*, *S. epidermidis*, *S.aureus*, *V. alginolyticus*, *E. faecalis*, *E. cloacae* and *E.coli*	MIC values: The concentration of 0.5 µg/mL for L.Monocytogens and S.epidermidis; higher concentrations need to inhibition of *S. aureus*, *V. alginolyticus*, and *S. enterica*, no inhibition effects against other bacteria, high soluble in water.	[39]
S-CS NPs	*S. sanguinis*, *S. aureus* and *E. faecalis*	MIC values: The concentration of 0.063, 0.135 and 0.284 mg/mL for *S. sanguinis*, *S. aureus*, and *E. faecalis*, respectively.	[40]
ZnO/Se NPs	*S. aureus*, and *E. coli*	100 µL of CS-ZnO/SeNPs provides an inhibition zone of 6.5 mm for *S. aureus* and an inhibition zone of 6 mm for *E. coli*, with higher antibacterial activity against *E. coli*.	[41]
Ag-chitosan nanocomposite	H_1N_1	Stronger antiviral activity in smaller NPs, Neat chitosan does not exhibit antiviral activity.	[42]
Selenium NPs with arbidol	H_1N_1	Preventing H_1N_1 infection by blocking DNA fragmentation and chromatin condensation, inhibiting hemagglutinin, neuraminidase and caspase-3 activity.	[43]
Oseltamivir-Selenium NPs	HCoV and MHV	Regulation of ROS and inhibition of cell apoptosis, strong adsorption of HCoV-NL63 virus, moderate adsorb of mouse hepatitis virus (MHV) and not adsorb HCoV-OC43 coronavirus.	[44]
Selenium- Chitosan Nanoparticles	H_3N_2	Inhibition of viral replication and overproduction of inflammatory cytokines, Inhibition of ROS production, regulation of apoptotic proteins affect the ROS/JNK pathway and reduce mitochondrial damage.	[45]

diameter (Z-average) and surface charge (zeta potential) of the nanoparticles produced at different rotation speeds were determined by DLS. Furthermore, the impact of elevating the concentration of reducing and stabilizing agents on the dimensions of nanoparticles was examined. To this end, the initial synthesis was augmented by an additional 10 mM of KI and ascorbic acid, and the particle hydrodynamic diameter was subsequently determined via a DLS/Zeta potential device. Also, the impact of the stabilizing agent (KI or CS), the diameter of the magnetic stirrer and the reaction time on the size of the Se NP has been investigated.

2.3 Preparation of Se-CS NPs and Se-CMCS NPs

The Se NPs were dispersed in deionized water. The CS and CMCS solutions were prepared at 10 mg/mL by adding 2 mL of acetic acid (1%) to 2 mL of distilled water. Subsequently, the Se NPs solution was divided into two 100 mL beakers, and 10 mL of the chitosan and CMCS solutions were added to the Se NPs colloidal dispersion under magnetic stirring (the coating was performed at a 1:2 ratio of Se NPs to CS/CMCS).

2.4 Preparation of Cur-CS NPs

An optimized chitosan-based drug delivery system was developed using the ionotropic gelation method [52]. In this process, 0.3 g of chitosan was dissolved in 100 mL of an acetic acid solution (2%), and the pH of the solution was adjusted to 5. Then, 1 mL of curcumin (dissolved in methanol at 500 µg/mL) was incorporated dropwise into the chitosan solution under constant stirring. Subsequently, a 0.1% (w/v) TPP solution was added dropwise to achieve a chitosan-to-TPP mass ratio of 3:1. The resulting suspension was stirred for 30 minutes at room temperature before being separated by centrifugation. The chitosan colloids were washed thoroughly with deionized water and air-dried [53].

2.5 Evaluation of the Encapsulation Efficiency of Cur-CS NPs

After the drug loading, the amount of encapsulated curcumin was assessed by centrifuging 3 mL of the nanostructure suspension at 13000 rpm for 10 minutes. The residual curcumin in the supernatant was quantified using UV spectrophotometry at 425-430 nm. The encapsulation efficiency (EE) was determined using the following equation:

$$\mathrm{EE}(\%) = \frac{\text{Total curcumin} - \text{Free curcumin}}{\text{Total curcumin}} \times 100$$

A standard curve was generated by preparing various concentrations of curcumin and measuring their absorbance at 425-430 nm.

2.6 Evaluation of curcumin release from Cur-CS NPs

The *in vitro* release profile of curcumin from the CS NPs was assessed using a dialysis bag method (12 kDa). Equal amounts of Cur-CS NPs were dispersed in 3 mL of pH-specific buffer (acetate buffer, pH 5 or PBS, pH 7.4, each containing 0.1% w/v Tween 80) and loaded into the dialysis bag. The sealed bags were immersed in 100 mL of a release medium (30% ethanol:70% buffer) and agitated at 180 rpm and 37 °C. At predetermined time intervals, 1 mL of the release medium was collected, and after each sampling, the volume was replaced with fresh medium. The absorbance of the collected samples was measured at 425-430 nm using a UV spectrophotometer. The concentration of the released drug was calculated based on a pre-established standard curve. The cumulative drug release was plotted as a function of time.

2.7 Antibacterial activity of Se-CS NPs and Se-CMCS NPs

The antibacterial activity of the nanosystem composed of stabilized Se-CS NPs/Se-CMCS NPs and Cur-CS NPs was evaluated using a disk diffusion test and the determination of zones of inhibition (ZOI) [38]. Sterile paper disks were impregnated with the same concentration of SeNPs, CS, CMCS, Curcumin, Cur-CS NPs, Se-CS NPs, Se-CMCS NPs, Se-CS@ Cur-CS NPs and Se-CMCS@ Cur-CS NPs placed on a freshly inoculated NA plate with individual bacterial cultures of *S. aureus* and *E. coli* after incubation of the plates for 24 h at 37 °C. The ZOI diameters and their standard deviations (± SDs) were calculated (all experiments performed in duplicate). Also, the microdilution method determined the MIC and MBC of the nanosystem. The broth microdilution method in 96-well microplates was used to measure the MIC of the solutions. Subsequently, exposed wells were treated with a TTC indicator solution to confirm bactericidal activity, as viable cells transformed TTC to a violet-red color [54]. Ampicillin and gentamicin antibiotics have been used as positive controls against *E. coli* and *S. aureus*, respectively [55].

2.8 Cell culture

Vero cell lines were subcultured and proliferated in DMEM containing FBS (10%) and antibiotics (100 IU/mL penicillin/streptomycin, Gibco) to form a uniform and stable monolayer cell culture (37 °C in a humidified atmosphere of 5% CO_2). Subsequently, the cells were subcultured via trypsinization (0.05%, Gibco).

2.9 SARS-CoV-2 strains

Clinical isolates of SARS-CoV-2, including the original Wuhan strain, have been isolated from nasopharyngeal swabs. This was determined by RT-PCR analysis of SARS-CoV-2 (GA SARS-CoV-2 OneStep RT-PCR kit) and confirmed by sequencing. Virus isolation and primary transfection were performed in Vero cells. SARS-CoV-2 was injected and replicated in Vero cells, and the degree of viral infection was calculated as the 50% tissue culture infectious dose (TCID50) using the Karber method [56]. All procedures were conducted in a Biosafety Level 3 (BSL-3) laboratory, and informed consent was obtained from all participants. Also, all methods were conducted in accordance with relevant guidelines and the study was performed under the following ethical codes applied in reference number 50 (protocols were approved by the National Research Ethics Committee): IR.NREC.1399.003, IR.NREC.1399.007, and IR.NREC.1399.008 [57].

2.10 SARS-CoV-2 virus neutralizing test

The conventional virus neutralization assay (cVNT) was conducted to assess the inhibitory activity of the hybrid nanosystem against SARS-CoV-2. Briefly, 50 µL of serially diluted NP colloids were mixed with 50 µL of SARS-CoV-2 (100 CCID50/mL) in DMEM and incubated at 37 °C for 1 hour. The resulting virus-NP suspensions were then transferred to monolayers of Vero cells ($1-2\times10^4$ cells/well in 96-well plates) and allowed to adsorb for 60 minutes at 37 °C. Following infection, the supernatant was aspirated, and the cell monolayers were rinsed twice with DMEM before being cultured in fresh DMEM for 48 hours at 37 °C under 5% CO^2. Viral cytopathic effects (CPE) were examined microscopically at 72 hours post-infection. The neutralizing titer of the NP colloids was defined as the highest dilution that completely prevented CPE formation. A neutralization potency below 1:4 was considered a negative result, while a titer of 1:4 or higher was scored as positive [57].

3. Results and discussion

3.1 Optimization and characterization of nanoparticles

The UV-Vis (Cary 100) spectrophotometer was used to validate the synthesis. The absorbance at 260 nm indicates the formation of Se NPs, and this peak is associated with the crystallinity of Se NPs [51]. Also, the DLS/Zeta potential tests (Zetasizer Nano ZS series, Malvern Instruments Ltd., UK) have been used to determine the surface charge and the size (hydrodynamic diameter) of nanoparticles. The results of various studies indicate that the size of Se NPs is the primary factor influencing their stability, antioxidant and antimicrobial activity. Consequently, it is essential to optimize the manufacturing process of these NPs to achieve smaller sizes [58]. Hence, an experimental design was used to evaluate the effect of the agitation speed (effect of rpm and magnetic stirrer size), the concentration of reductant and stabilizer, reaction time and type of stabilizing agent on the size of the NPs. The FTIR (Nicolet IR 100) analysis extracts functional groups related to each step of the synthesis process. The XRD (Philips X′Pert MPD, 40 kV, $\lambda = 1.54056$ Å) provides information about a material's crystallographic structure and physical properties. FE-SEM (Mira 3-XMU) and TEM (Zeiss-EM10C, 100 kV) provide essential results regarding nanoparticle size, morphology and size distribution.

The color suspension of the NPs directly reflects their dimensions. According to a method for evaluating the size of Se NPs by UV-Vis spectra, the suspension of Se NPs with a 20 nm diameter shows a yellowish-orange appearance and an absorption maximum below 250 nm. However, with increasing the particle size, a redshift occurred in the absorption peak maxima and an absorption maximum below 350 nm indicated the Se NPs suspension with diameters of about 100 nm. In comparison, for Se NPs with a size of 240-280 nm, the absorption maximum was recorded at 680 nm [59]. As shown in figure 1 A, the absorption peak at 260

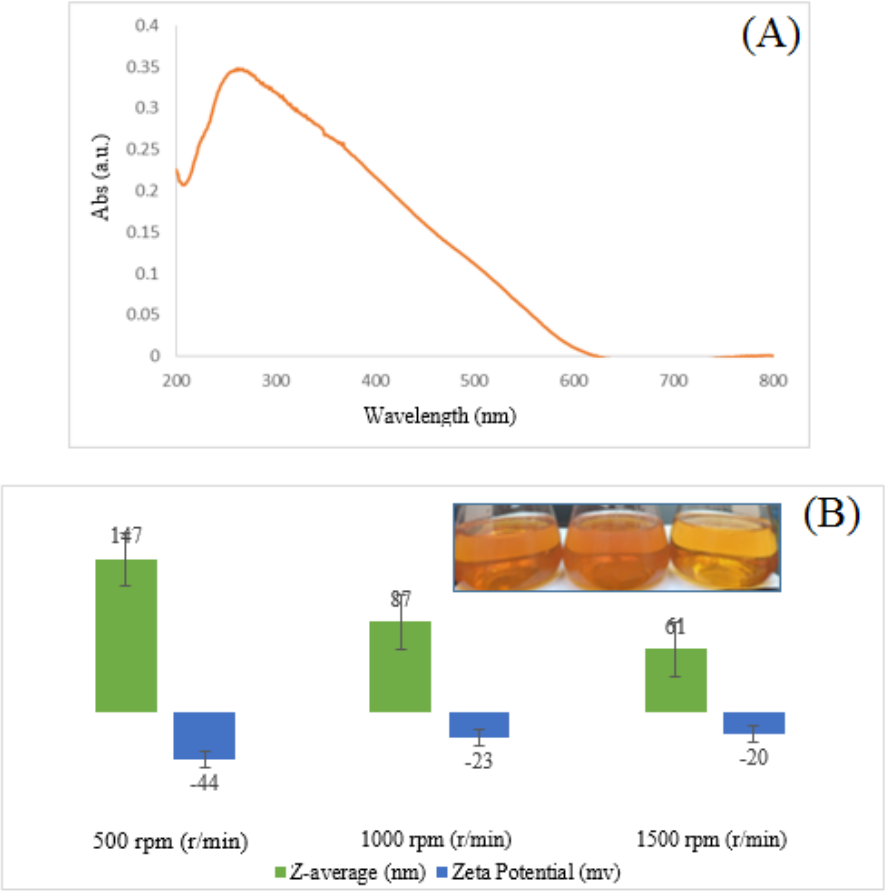

Figure 1. (A) UV-Vis spectra, and (B) The effect of the rpm factor on the size and charge of Se NPs.

nm confirms the presence of Se NPs [60]. Also, increasing the rpm from 500-1500 r/min decreased the NP size from 147 nm to 61 nm. Furthermore, the absolute value of the negative surface charge of NPs has been significantly diminished (figure 1 B). This issue can be attributed to the speed of agitation of materials in the baker. In addition to the influence of rotation speed on NPs size, several main factors were also manipulated, including the stabilizer agent (KI or CS), the concentration of KI and ascorbic acid, the diameter of the magnet stirrer, and reaction time. Increasing the KI (40 mM) and ascorbic acid (70 mM) concentration causes the production of smaller NPs. In addition, the larger magnetic stirrer yielded smaller nanoparticles compared to the smaller magnetic stirrer (Table 2). In contrast, using CS instead of KI as a stabilizing agent during the synthesis of Se NPs resulted in the formation of NPs with a significantly larger size ($>$ 250 nm). The results also showed that increasing the reaction time had no effect on the size change of the Se NPs and these findings are in line with those reported by Sentkowska and Pyrzynska, and Suriati et al. [61, 62].

Although few studies have examined the effects of reducing agent and stabilizer concentrations on Se NP size, studies on silver NPs showed that increasing the concentrations of the reducing agent and stabilizer to a certain level can produce smaller NPs [62, 63]. So, in relation to Se NP, this reduction in NP size, observed with increasing concentrations of ascorbic acid (reducing agent) and potassium iodide (stabilizer), can be attributed to the following: In this synthesis process, after sodium selenite salt dissolves in water, a large number of selenite ions are released into the environment. It is expected that the higher the concentration of the reducing agent, the faster the reduction proceeds, resulting in smaller Se NPs. Furthermore, increasing the stabilizer concentration prevents NPs from agglomerating and growing in size during the synthesis reaction. This variation in particle size significantly impacted the color of the solutions containing them. The solutions comprising smaller NPs exhibit a bright yellow hue. This phenomenon can be explained by an increase in the energy band gap in smaller NPs, while the orange color of solutions containing larger nanoparticles can indicate a decrease in the energy band gap [64].

The absence of a protective coating on the surface led to aggregation of the Se NPs via van der Waals forces between particles, which dominated the assembly process. This uncontrolled aggregation prevented the formation of monodisperse Se nanospheres. To prevent aggregation, the Se NPs should be stabilized by a coating agent. The synthesized NPs were coated using CS and CMCS [65]. Following the coating with a similar CS and CMCS concentration, the average hydrodynamic diameters increased to 92 nm and 103 nm, respectively. Furthermore, the presence of the NH_3 group on the surface of the synthesized NPs provides a positive surface charge, with values of +45 mV for Se-CS NPs and +17 mV for Se-CMCS NPs. The notable expansion in the dimensions of NPs modified with CMCS can be attributed to the high repulsion of the polymeric chains at higher pH. In contrast, the number of ammonium/hydronium ions and water absorption decreases for CS. Additionally, the presence of COOH functional groups in CMCS resulted in a lower zeta potential for Se-CMCS NPs than for Se-CS NPs (figure 2).

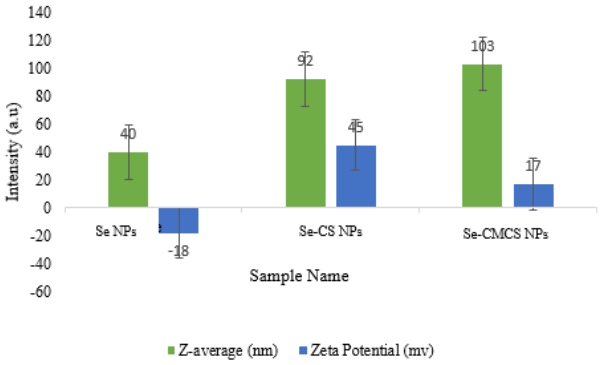

Figure 2. The comparison of the size and charge at Se NPs, Se-CMCS NPs and Se-CS NPs.

Also, the uniform morphology of NPs with a sphere shape was shown in the FE-SEM image. Based on the FE-SEM image, Se-CS NPs are smaller than Se-CMCS NPs (figure 3). TEM was done to determine the size of NPs and validate the core-shell structures. As shown in figure 4, the core-shell structure is evident in both the CS and CMCS coatings. NPs are uniform and have the same sphere morphology, and the size of Se-CS NPs and Se-CMCS NPs is estimated at 73 nm and 80 nm, respectively.

The FTIR analysis has been performed to confirm the presence of CS and CMCS functional groups in the structure. As shown in figure 5 A, the prominent absorption bands of the Se NPs were at 3415 cm^{-1} (O-H stretch), 2353 cm^{-1} (C-H

Table 2. Evaluating the effects of KI/ascorbic acid concentration, and magnetic stirrer size on Se NPs' Z-average and charge.

Sample	Z-average (nm)	Zeta (mv)
First synthesis (rpm 1500)	61.63	−20
Increasing of KI	58.43	−4.93
Increasing of ascorbic acid	54.39	3.29
Increasing of KI and ascorbic acid	47.41	−6.84
Increasing of magnetic stirrer size	56.03	−1.41
Increasing of KI and ascorbic acid + large magnet + rpm 1500	40.53	−18

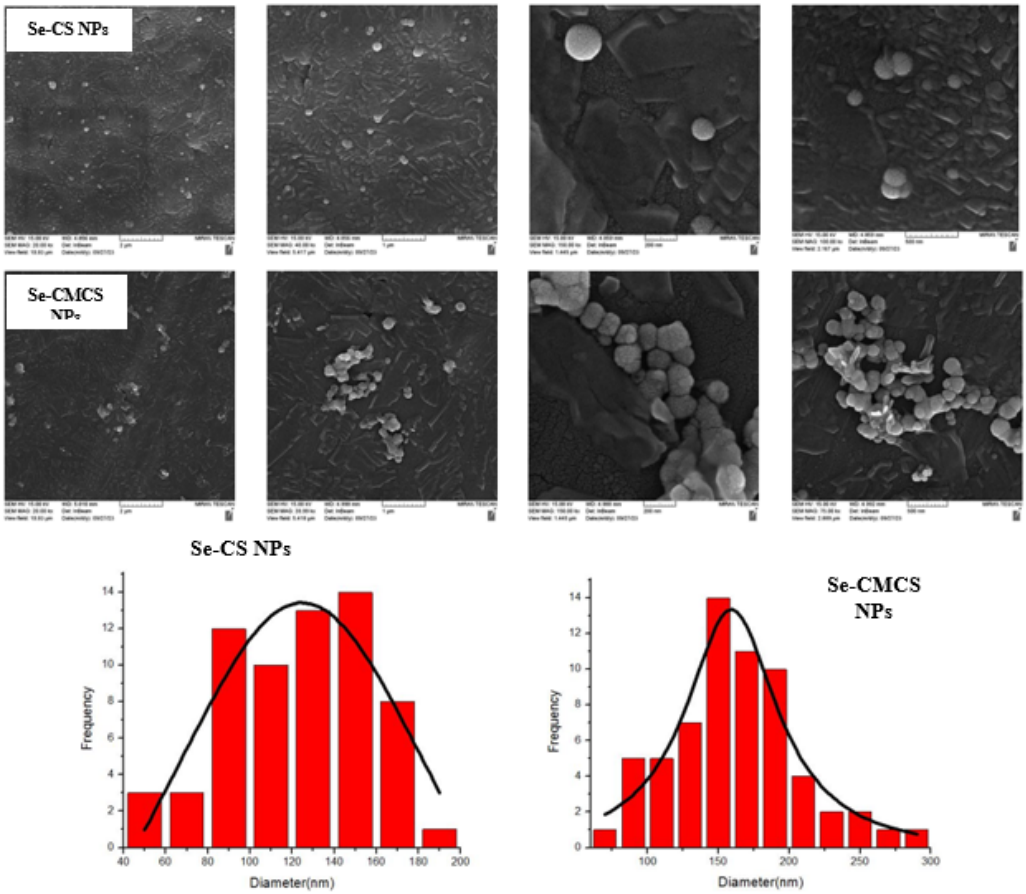

Figure 3. The Fe-SEM image of Se-CS NPs, Se-CMCS NPs and the particle size distribution histogram based on Fe-SEM images.

stretch), 1624 cm^{-1} (C=O stretch or O-H bend), 1381 cm^{-1} (C-H bend) and 610 cm^{-1} (Se-O and Se-Se). The main absorption bands of CS were at 3428 cm^{-1} (O-H stretch), 2362 cm^{-1} (C-H stretch), 1660 cm^{-1} (C=O stretch), 1588 cm^{-1} (N-H bend), 1352 cm^{-1} (C-H bend), 1078 cm^{-1} (C-O stretch). The observation of CS functional groups in the Se-CS NPs spectrum confirms the presence of this substance within the structure. Moreover, the characteristic peak of the O-H group in Se-CSNPs was observed to be shifted compared to that of CS, with a value of 3407 cm^{-1}. The absorption peaks of CMCS were 3419 cm^{-1} (O-H stretch), 2360 cm^{-1} (C-H stretch), 1630 cm^{-1} (C=O stretch and -COO stretch) and 1084 cm^{-1} (C-O stretch). While the characteristic absorption peaks of the hydroxyl group of CMCS were at 3419 cm^{-1}, the peak shifted to 3426 cm^{-1} in Se-CMCS NPs. The observed shift in the O-H band indi-

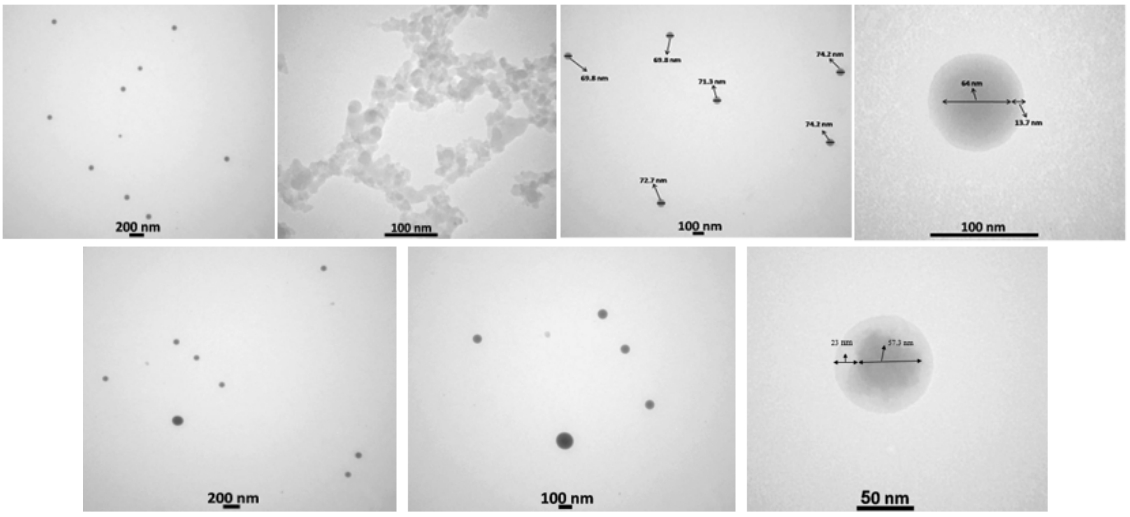

Figure 4. The TEM image of Se-CS NPs and Se-CMCS NPs.

cates the formation of an interaction between the hydroxyl groups of CS/CMCS and the surface of Se NPs [66]. Also, the FTIR spectra of curcumin were attributed to functional groups such as 3440 cm^{-1} (free –OH group), 2950 cm^{-1} (C-H stretching of the aromatic ring), 2300 cm^{-1} (C-H stretching of the methyl group), 1634 cm^{-1} (C=O, C=C), 1450 cm^{-1} (aromatic C=C), 1260 cm^{-1} (CH_2 bending), and 1099 cm^{-1} (CH_3 bending). For the Cur-CS NPs (a hydrodynamic diameter of 156 nm and a surface charge of +25 mV), the prominent peaks were observed at 3414 cm^{-1} (free –OH group), 2930 cm^{-1} (C-H stretching of the methyl group), 1643 cm^{-1} (C=O, C=C), 1530 cm^{-1} (aromatic C=C), 1426 cm^{-1} (CH_2 bending), and 1075 cm^{-1} (CH_3 bending) [37]. The FTIR analysis revealed the presence of all peaks associated with curcumin and chitosan. Notable wavenumber shifts were observed in the main peaks related to curcumin (–OH, C=O, and aromatic C=C), confirming the successful fabrication of Cur-CS NPs. These shifts are often attributed to hydrogen bonding, electrostatic interactions, or encapsulation effects between curcumin and chitosan (figure 5 B).
In addition, the XRD pattern shows the synthesis of Se NPs and the addition of CS and CMCS on the surface of NPs (Figure 5C). The characteristic peak at 2θ values of 23.4°, 29.2°, 34.5°, 35.8°, 38.1° and 47.2° indicates their crystalline nature and reduction from selenite ions present in the medium [67]. Moreover, the XRD pattern indicates that coating Se NPs reduces their crystallinity, with the effect more pronounced in those coated with CMCS. The Debye-Scherer equation was used to determine the average crystallite size [68]:

$$D = \frac{K\lambda}{\beta_{hkl}\cos\theta} \tag{1}$$

where D, K, and λ are crystallite size, shape factor (0.94), and wavelength of Cukα radiation, respectively [66, 69].
From the calculations, the average crystallite sizes of the Se NPs, Se-CS NPs, and Se-CMCS NPs are 37.2, 25.2, and 3.8 nm, respectively.
The Scherer method assumes that peak broadening arises solely from finite crystallite dimensions, neglecting the influence of lattice strain. In contrast, the Williamson-Hall approach deconvolutes the total broadening into separate size and strain components. This approach provides a more comprehensive microstructural analysis by quantifying both the average crystallite size and the strain present [70, 71]. So, based on the Williamson-Hall equation:

$$\beta_{hkl}\cdot\cos\theta = \frac{K\lambda}{D} + 4\varepsilon\sin\theta \tag{2}$$

A plot is drawn with $4\varepsilon\sin\theta$ along the x-axis and $\beta_{hkl}\cdot\cos\theta$ along the y-axis (Hall plot). From the linear fit to the data, the crystallite size and strain were estimated from the y-intercept ($K\lambda/D$) and slope (ε), respectively. The fitted line gives the equation ($y = -0.0005x + 0.0053$) with the intercept 0.0053 [72]. rom these data, the crystallite sizes of the Se NPs, Se-CS NPs, and Se-CMCS NPs are 39.4, 26.8, and 6.1 nm, respectively.
Generally, considering that the crystallite size obtained from two equations is smaller than the size of the particles obtained from TEM, many crystals may be combined to form NPs. Furthermore, the DLS analysis was performed to assess the stability of NPs, and the size change of Se-CS NPs and Se-CMCS NPs was examined over time. After four months of storage at 4 °C, the DLS size of Se NPs underwent a notable change, increasing from 40 to 273 nm. In contrast, the size of Se-CS NPs and Se-CMCSNPs exhibited a slight shift from 92 to 107 and 103 to 123 nm, respectively (figure 6). Moreover, following approximately one year of storage at 4 °C, the dimensions of Se-CS NPs and Se-CMCS NPs have been established at 114 and 142

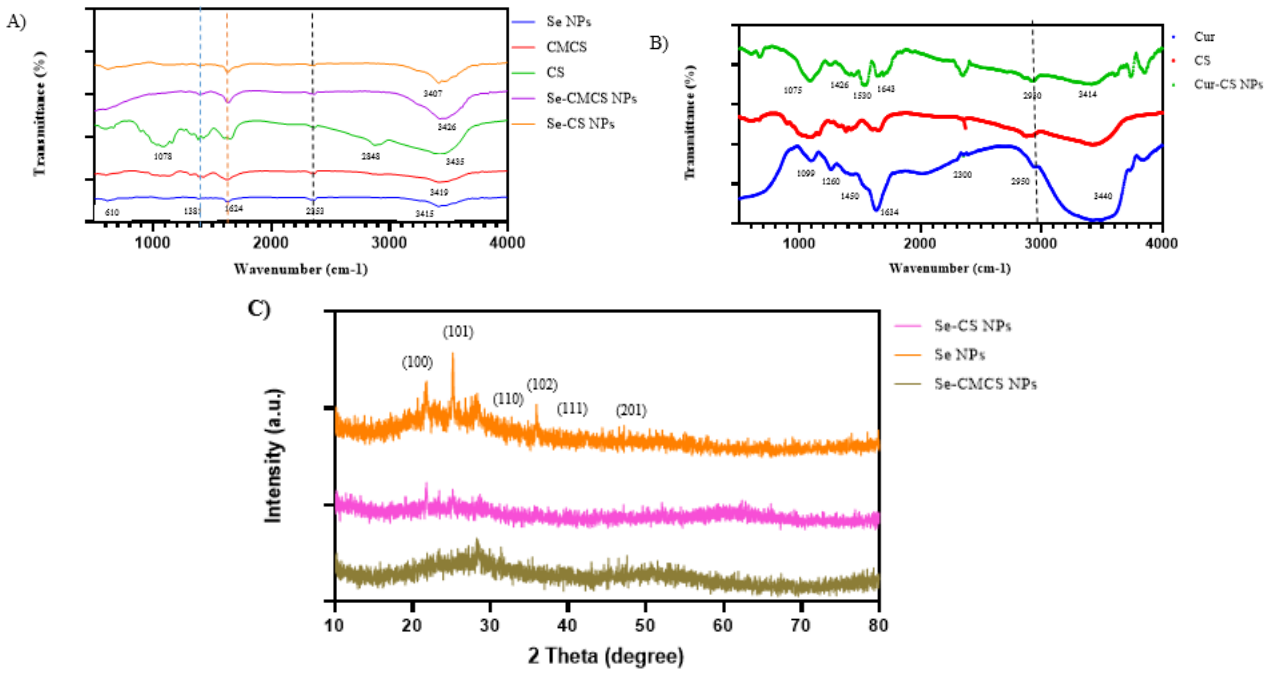

Figure 5. (A) The FTIR spectra of Se NPs, CS, CMCS, Se-CS NPs and Se-CMCS NPs, (B) The FTIR spectra of Cur, CS, Cur- CS NPs, (C) The XRD Pattern of Se NPs, Se-CS NPs and Se-CMCS NPs.

nm, respectively. This increase in the size of Se-CMCS NPs compared to Se-CS NPs can be attributed to the synthesis of the Se NPs in an aqueous medium and to CMCS's high water permeability. Also, due to the lower zeta potential and the resulting lower positive surface charge of Se NPs synthesized with CMCS (+17 mV) compared to those synthesized with CS (+45 mV), the repulsion between nanoparticles decreases, leading to their eventual aggregation over time.

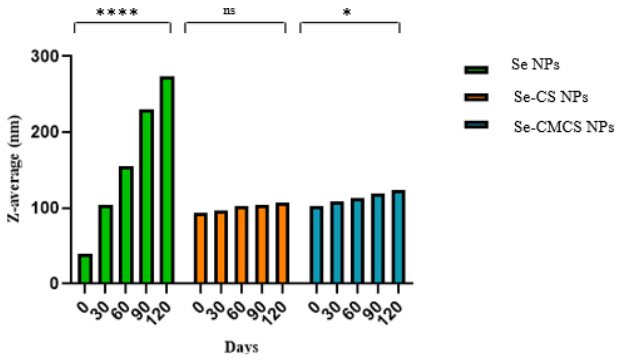

Figure 6. The changes of the Se NPs, Se-CS NPs and Se-CMCS NPs size after four months.

3.2 Encapsulation efficiency and drug release study of curcumin

The encapsulation efficiency was determined using a standard curcumin curve, and the percentage of curcumin encapsulated within the chitosan nanoparticles was greater than 80%. In addition, the drug release of curcumin from the Cur-CS NPs was evaluated under simulated physiological (pH 7.4) and acidic (pH 5) conditions. The release profile exhibited a controlled, sustained release pattern devoid of an initial burst, indicating successful and homogeneous curcumin encapsulation within the nanoparticle core (figure 7). Analysis over 48 hours revealed a pH-dependent release, with 45% of the drug released at pH 5 compared to 30% at pH 7.4. This disparity is attributed to the pH-responsive swelling of the chitosan matrix. At lower pH, enhanced protonation facilitates polymer hydration and swelling, promoting medium penetration and a transition to a rubbery state that accelerates drug diffusion. The superior release at pH 5 may be further enhanced by curcumin's greater stability in acidic media. Therefore, it is anticipated that these nanoparticles can deliver an adequate concentration of curcumin within infectious, acidic microenvironments to inhibit pathogen growth.

3.3 Evaluation the antibacterial activity

A review of recent studies indicates that NPs exhibit antimicrobial activity against various microbial infections. The small particle size and charged surface of NPs provide an accessible route for entry into pathogenic cells, enabling interference with cellular contents such as proteins and DNA, thereby inducing programmed cell death. Several mechanisms have been described for the antibacterial activity of Se NPs, including the generation of reactive oxygen species (ROS), disruption of the cell barrier, and inhibition of protein synthesis and DNA. The ROS species can damage bacterial cell membranes and inhibit DNA replication

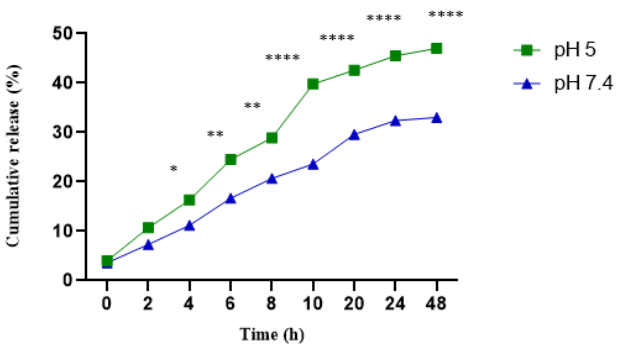

Figure 7. Cumulative curcumin release from the Cur-CS NPs over time at pH 7.4 and pH 5.

or amino acid synthesis [73, 74] (figure 8). Muchova et al. investigated the impact of Se NPs with a size range of 100-200 nm on the antibacterial efficacy of a collagen-chitosan scaffold. Their findings indicate that Se NPs enhanced the antibacterial activity against *S. aureus* and MRSA at concentrations between 0.5 µg/mL and 5 µg/mL [75]. Additionally, Dorazilova et al. demonstrated that the scaffold contains Se-CS NPs and Se-carboxymethyl cellulose NPs at concentrations < 5 µg/mL, which exhibited a pronounced antibacterial effect, with up to 94% inhibition of bacterial growth [76]. Elmaaty et al. employed Se NPs with a size range of 36-150 nm to fabricate polyester fabric and leather materials. Their findings demonstrated a notable killing potential against both Gram-positive and Gram-negative bacteria, as well as an ability to impede the transmission of bacterial infection facilitated by humidity, temperature and poor breathability [77, 78]. Moreover, Mao et al. utilized a nanocomposite hydrogel comprising bacterial cellulose, gelatin, and Se NPs (75 nm). They showed that the nanocomposite, at a concentration of 65.44 µg/mL, can inhibit bacterial infection and accelerate skin regeneration in a clinical setting [79]. This study evaluated the antibacterial activities of Se NPs, Se-CS NPs, Se-CMCS NPs, Cur-CS NPs, Se-CS@Cur-CS NPs and Se-CMCS@Cur-CS NPs against *E. coli* and *S. aureus*. The disk diffusion method and MIC/MBC tests were used to determine the antibacterial effects. Our findings demonstrate that both nanosystems, Se-CS@Cur-CS NPs and Se-CMCS@Cur-CS NPs, exhibit significant antibacterial effects, and the data presented in Table 3 substantiate the synergistic impact of Se NPs, curcumin, and chitosan derivatives. Additionally, the MIC/MBC results for Se-CS@Cur-CS NPs and Se-CMCS@Cur-CS NPs showed notable similarity, and both NPs at concentrations of 0.570-1.251 µg/mL inhibited the growth of *E. coli* and *S. aureus*, respectively. Also, these NPs at concentrations of 1.251 µg/mL and 9.251 µg/mL can show bactericidal effects against *E. coli* and *S. aureus*, respectively.

3.4 Evaluation of antiviral activity against SARS-CoV-2

In the context of the emergence of SARS-CoV-2, there has been a notable increase in the utilization of Se NPs in various biomedical applications, including antibacterial, antiviral, and antifungal agents, from 2019 to the present [58].

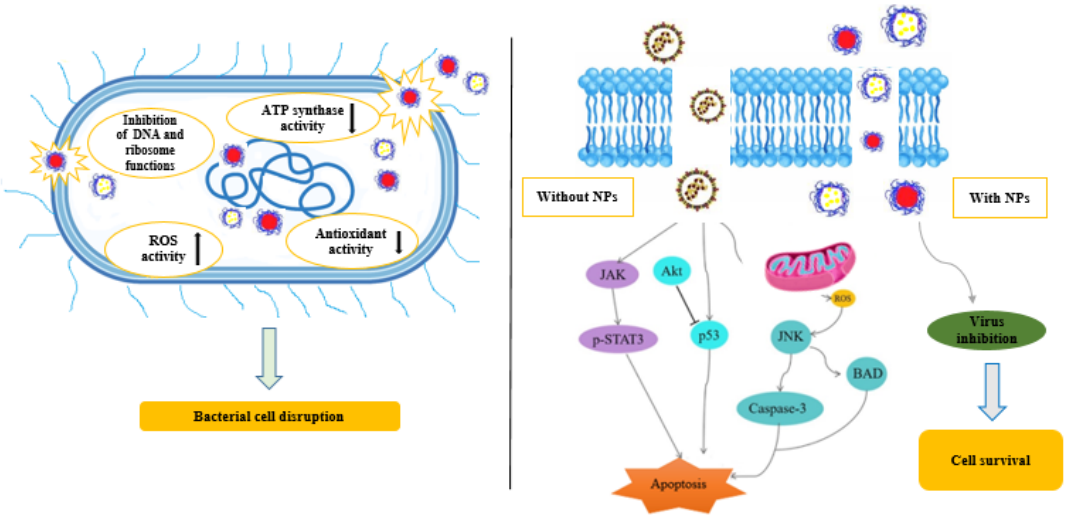

Figure 8. Schematic of the proposed antibacterial and antiviral mechanisms of the synthesized NPs.

In SARS-CoV-2, the spike protein binds to the angiotensin-converting enzyme 2 (ACE2) receptor on the surface of human cells and enables viral entry via endocytosis. Consequently, targeting viral attachment to the ACE2 receptor or impeding viral endocytosis is a promising therapeutic strategy for drug development and combating COVID-19. Several mechanisms perform the antiviral activity of Se NPs: disruption of viral capsid proteins, the inhibition of ROS production, the regulation of apoptotic proteins (JNK, P53, caspase-3, JAK, p-STAT3, and Akt), the modulation of the ROS/JNK pathway, the reduction of mitochondrial damage, inhibition of viral replication and improving the efficiency of antiviral drugs (figure 8). Furthermore, Se-CS NPs have been demonstrated to impede the excessive production of inflammatory cytokines in infected cells and mitigate the inflammatory response associated with viral infection [45]. Touliabah et al. demonstrated that Polycadia myrica-mediated Se NPs (PoSe NPs) exhibit robust antiviral activity against the HAV-10 virus, with an antiviral percentage of 40.25%. However, the antiviral activity of PoSe NPs against adenovirus and HSV-2 was comparatively weaker, with antiviral percentages of 8.64% and 17.39%, respectively [80]. Also, Zhong et al. indicated that the oseltamivir-functionalized Se NPs were effectively internalized by human astrocyte U251 cells (host cells) via clathrin-mediated endocytosis, leading to the inhibition of Enterovirus 71 (EV71) proliferation. This process could protect virus-infected cells from apoptosis through the mitochondrial pathway. Moreover, these NPs demonstrated the capacity to inhibit viral activity by reducing the generation of reactive oxygen species in infected cells while simultaneously enhancing the antiviral activity of oseltamivir in the anti-EV71 cell model [81].

In our study, the toxicity results indicate that using NPs below 110 µg/mL has no toxic effects. However, at concentrations above this threshold, the inhibitory effects of NPs on cell proliferation and survival become apparent. Then, the VNT test was performed to evaluate the antiviral effects of the same concentrations of Se-CS@Cur-CS NPs and Se-CMCS@Cur-CS NPs against SARS-CoV-2.

The results of the VNT indicate that Se-CS@Cur-CS NPs begin to reduce the infectivity of SARS-CoV-2 at a dilution of 1:64. Additionally, the Se-CMCS@Cur-CS NPs trigger virus inhibition at a dilution of 1:32. The results demonstrate that Se-CS@Cur-CS NPs exhibit enhanced antiviral properties at equivalent concentrations compared to Se-CMCS@Cur-CS NPs (figure 9). Subsequently, dilutions 101 to 106 were prepared from the virus and the

Table 3. The results of the disk diffusion method.

Nanoparticles	ZOI for *E. coli* (mm)	ZOI for *S. aureus* (mm)
Se NPs	2.5 ± 0.5	-
CS	4.3 ± 1	1.1 ± 1
CMCS	4 ± 1	1.5 ± 1
Curcumin	2.7 ± 0.5	1.2 ± 0.5
Cur-CS NPs	4.6 ± 1	1.5 ± 1
Se-CS NPs	5.2 ± 0.5	1.3 ± 0.5
Se-CS@Cur-CS NPs	5.5 ± 1	1.7 ± 0.5
Se-CMCS NPs	5.1 ± 0.5	1.5 ± 0.5
Se-CMCS@Cur-CS NPs	5.6 ± 0.5	2.1 ± 1

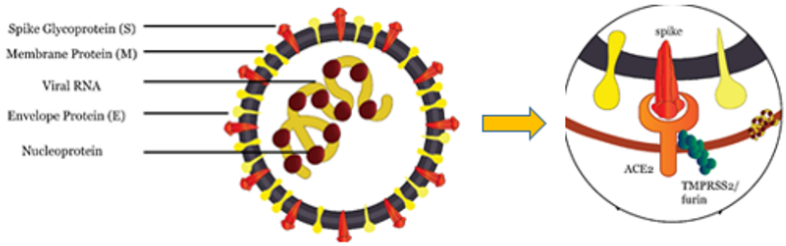

Serial Dilution of NP Solutions	1:2	1:4	1:8	1:16	1:32	1:64	1:128	1:256	1:512	1:1024	1:2048
Se-CS@Cur-CS NPs	+	+	+	+	+	+	-	-	-	-	-
Se-CMCS@Cur-CS NPs	+	+	+	+	+	-	-	-	-	-	-
Controls											
Positive Control 1	+	+	+	+	+	+	+	+	+	+	-
Positive Control 2	+	+	+	+	+	+	+	+	+	-	-
Negative Control 1	-	-	-	-	-	-	-	-	-	-	-
Negative Control 2	-	-	-	-	-	-	-	-	-	-	-

Figure 9. SARS-CoV-2 structure and the antiviral activity of Se-CS@Cur-CS NPs and Se-CMCS@Cur-CS NPs at various dilutions.

Se-CS@Cur-CS NPs were found capable of neutralizing the first two flasks. However, the neutralization effects were also observed in dilution 103 in a subsequent experiment. Figure 10 depicts the light microscopic images of control cells after treatment with SARS-CoV-2 incubated with stabilized Se-CS@Cur-CS NPs and Se-CMCS@Cur-CS NPs. As illustrated in the picture, using Se-CS@Cur-CS NPs at a dilution of 1:64 yields high cell viability and a confluence exceeding 80%. Additionally, for Se-CMCS@Cur-CS NPs a dilution of 1:32, significant cell survival with normal morphology and a confluence of more than 70% is observed. Conversely, in samples with lower concentrations of stabilized NPs, the cells were infected with the virus, leading to cell death. So, our findings demonstrate that both Se NPs stabilized with CS/CMCS combined with Cur-CS NPs exhibit similar antimicrobial activity against *E. coli* and *S. aureus*. However, in neutralizing SARS-CoV-2, the nanosystem composed of Se-CS combined with Cur-CS shows significantly superior antiviral efficacy compared to the alternative nanosystem. Based on available research, the SARS-CoV-2 virus has a negative surface charge overall, primarily due to its spike (S) protein. Cotten and Phan demonstrate that the original Wuhan strain had a charge of approximately -8.3, which evolved to around -1.26 in many Omicron variants [82]. Therefore, in the nanosystem containing Se-CS NPs with a higher positive surface charge ($+45$) compared to the nanosystem containing Se-CMCS NPs with a lower positive surface charge ($+17$), a

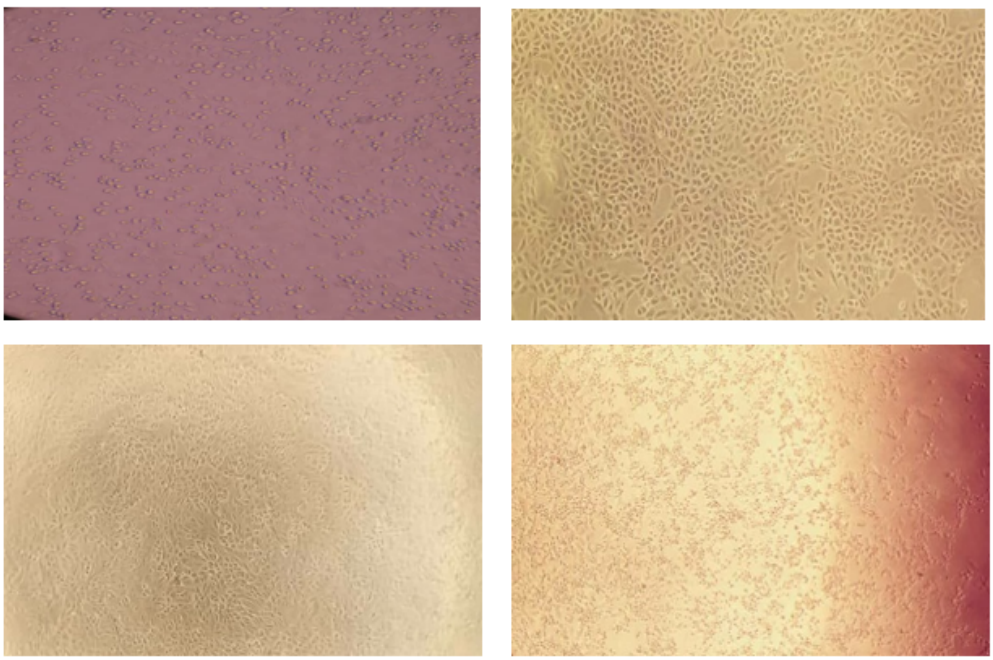

Figure 10. The light microscopic images of (A) The SARS-CoV-2 infected Vero cells, (B) Vero cells after SARS-CoV-2 incubation with a dilution of 1:64 of Se-CS@Cur-CS NPs, (C) Vero cells after SARS-CoV-2 incubation with a dilution of 1:32 of Se-CMCS@Cur-CS NPs, (D) Vero cells after SARS-CoV-2 incubation with the Se-CMCS@Cur-CS NPs at dilutions $\leq$ 1:32.

greater inhibitory effect on the virus is expected. This inhibitory effect can be attributed to electrostatic interactions between the CS containing NPs and the negatively charged viral spike glycoprotein. These interactions can effectively prevent the binding of the spike glycoprotein to the ACE2 receptor, thereby inhibiting viral entry into the host cell. Furthermore, this nanosystem can, through another mechanism, directly damage the viral envelope, ultimately leading to its inactivation. So, the results indicated that incorporating these small NPs into various detergents and cosmetic products could help prevent the prevalence and spread of infectious pathogens. Furthermore, the use of these NP colloids has the potential to accelerate the healing process in patients. So, incorporating nanomaterials into products such as mouthwash, toothpaste, hand sanitizers, and nasal sprays presents a highly effective approach for combating pathogens. Additionally, this study presents a practical strategy for reducing the transmission and progression of infectious diseases.

4. Conclusion

Microorganisms are a leading cause of infectious diseases, resulting in substantial global health and economic burdens. Se, an essential trace element, has been shown to exhibit antibacterial, antiviral, and anticancer properties. However, Se NPs tend to precipitate quickly and require stabilization using biocompatible coating agents, such as chitosan and its derivatives. The size of NPs plays a critical role in their antimicrobial efficacy. After one year of storage at 4 °C, the dimensions of Se-CS NPs and Se-CMCS NPs were measured at 114 nm and 142 nm, respectively. Our research indicates that higher rotation speeds, larger magnetic stirrer and increased concentrations of ascorbic acid and KI lead to smaller NPs forming. Conversely, substituting KI with CS as a stabilizing agent during Se NP synthesis results in larger NPs, while reaction time does not significantly affect NP size.

Additionally, Cur-CS NPs were synthesized by ionotropic gelation, achieving high encapsulation efficiency. The NPs exhibited pronounced pH-dependent release. The synergistic combination of Se NPs and curcumin employs two complementary antimicrobial mechanisms, selenium ion release and polyphenolic activity, yielding more comprehensive and longer-lasting effects than single-component systems. Specifically, Se-CS@Cur-CS NPs and Se-CMCS@Cur-CS NPs at concentrations of 0.570-1.251 µg/mL effectively inhibited the growth of *E. coli* and *S. aureus*. These nanosystems also demonstrated similar bactericidal activity at 1.251 µg/mL and 9.251 µg/mL against *E. coli* and *S. aureus*. Notably, the nanosystem components were non-toxic at concentrations below 110 µg/mL for Vero cells. Furthermore, Se-CS@Cur-CS NPs and Se-CMCS@Cur-CS NPs effectively prevented SARS-CoV-2 infection at high dilutions of 1:64 and 1:32, respectively. Its scalable production and dual antibacterial/antiviral action tackle antimicrobial resistance and viral threats. In conclusion, this study presents a scalable, biocompatible nanosystem with significant potential to address drug-resistant pathogens and viral threats through targeted therapeutic applications. Acknowledgment Tarbiat Modares University supported the present study.

Authors Contribution
All authors have contributed equally to prepare the paper.

Availability of data and materials
The datasets generated during and/or analyzed during the current study are available from the corresponding author on reasonable request.

Conflict of interests
The authors declare that they have no known competing financial interests or personal relationships that could have appeared to influence the work reported in this paper.

References

[1] Y. F. Avval, G. B. Pour, and M. M. Aram. Fabrication of high efficiency coronavirus filter using activated carbon nanoparticles. *International Nano Letters*, **12**:421–6, (2022).

[2] B. Hu, H. Guo, P. Zhou, and Z.-L. Shi. Characteristics of SARS-CoV-2 and COVID-19. *Nature Reviews Microbiology*, **19**:141–54, (2021).

[3] D. Efrain Merma Chacca, I. Maldonado, and F. Z. Vilca. Environmental and ecotoxicological effects of drugs used for the treatment of COVID 19. *Frontiers in Environmental Science*, **10**:940975, (2022).

[4] T. C. Ezike, U. S. Okpala, U. L. Onoja, C. P. Nwike, E. C. Ezeako, O. J. Okpara, et al. Advances in drug delivery systems, challenges and future directions. *Heliyon*, **9**(6), (2023).

[5] E. Blanco, H. Shen, and M. Ferrari. Principles of nanoparticle design
Biotechnology, **33**:941–51, (2015).

[6] R. Medhi, P. Srinoi, N. Ngo, H.-V. Tran, and T. R. Lee. Nanoparticle-based strategies to combat COVID-19. . *ACS Applied Nano Materials*, **3**:8557–80, (2020).

[7] Z. Tavakoli, F. Yazdian, F. Tabandeh, and M. Sheikhpour. Regenerative medicine as a novel strategy for AMD treatment: A review. *Biomedical Physics & Engineering Express*, **6**:012001, (2019).

[8] Z. Rezaei and B. Ranjbar. Ultra-sensitive, rapid gold nanoparticle-quantum dot plexcitonic self-assembled aptamer-based nanobiosensor for the detection of human cardiac troponin I. *Engineering in Life Sciences*, **17**:165–74, (2017).

[9] H. S. Abbas, A.M. Mahmoud, R. A. Wahed, M. A. A. Elsantawy, N. M. Hamdy, S. E. Ismail, et al. Prospects of using bioactive compounds in nanomaterials surface decoration and their biomedical purposes. *International Nano Letters*, **12**:125–38, (2022).

[10] Z. Ghalanbor, S.-A. Marashi, and B. Ranjbar. Nanotechnology helps medicine: nanoscale swimmers and their future applications. *Medical Hypotheses*, **65**:198–9, (2005).

[11] M. S. de Almeida, E. Susnik, B. Drasler, P. Taladriz-Blanco, and A. Petri-Fink. Rothen-Rutishauser B. Understanding nanoparticle endocytosis to improve targeting strategies in nanomedicine. *Chemical Society Reviews*, **50**:5397–434, (2021).

[12] L. S. Ardekani, T. T. Moghadam, P. W. Thulstrup, and B. Ranjbar. Design and fabrication of a silver nanocluster-based aptasensor for lysozyme detection. *Plasmonics*, **14**:1765–74, (2019).

[13] B. Lallo da Silva, M. P. Abuçafy, E. Berbel Manaia, and J. A. Oshiro Junior. Chiari-Andréo BG, Pietro RCR, et al. Relationship between structure and antimicrobial activity of zinc oxide nanoparticles: An overview. *International Journal of Nanomedicine*, **2019**: 9395–410, (2019).

[14] N. Rezapour, B. Rasekh, S. R. Mofradnia, F. Yazdian, H. Rashedi, and Z. Tavakoli. Molecular dynamics studies of polysaccharide carrier based on starch in dental cavities. *International Journal of Biological Macromolecules*, **121**:616–24, (2019).

[15] P. K. Sarkar and C. Das Mukhopadhyay. Ayurvedic metal nanoparticles could be novel antiviral agents against SARS-CoV-2. . *International Nano Letters*, **11**:197–203, (2021).

[16] M. Xie, M. Gao, Y. Yun, M. Malmsten, V. M. Rotello, R. Zboril, et al. Antibacterial nanomaterials: mechanisms, impacts on antimicrobial resistance and design principles. *Angewandte Chemie International Edition*, **62**:e202217345, (2023).

[17] Z. Hallaji, Z. Bagheri, S.-O. Kalji, E. Ermis, and B. Ranjbar. Recent advances in the rational synthesis of red-emissive carbon dots for nanomedicine applications: A review. *FlatChem*, **29**:100271, (2021).

[18] M. Iqbal, A. Ibrar, A. Ali, F. H. Memon, F. Rehman, Z. Bhatti, et al. Facile synthesis of zinc oxide nanostructures and their antibacterial and antioxidant properties. *International Nano Letters*, **12**:205–13, (2022).

[19] M. Maliki, I. H. Ifijen, E. U. Ikhuoria, E. M. Jonathan, G. E. Onaiwu, U. D. Archibong, et al. Copper nanoparticles and their oxides: optical, anticancer and antibacterial properties. . *International Nano Letters.*, **12**:379–98, (2022).

[20] S. Mohammadi, K. Khajeh, M. Taghdir, N. Farahani, and B. Ranjbar. Spectroscopic Studies on the Interaction of Gold Nanoparticles with Lysozyme. *Biomacromolecular Journal*, **5**:140–51, (2019).

[21] Z. Hallaji, Z. Bagheri, and B. Ranjbar. The role of fluorescent carbon dots in the fate of plastic waste. . *Journal of Environmental Chemical Engineering*, **11**:110322, (2023).

[22] Z. Hallaji, Z. Bagheri, M. Oroujlo, M. Nemati, Z. Tavassoli, and B. Ranjbar. An insight into the potentials of carbon dots for in vitro live-cell imaging: recent progress, challenges, and prospects. *Microchimica Acta*, **189**:190, (2022).

[23] N. Bisht, P. Phalswal, and P. K. Khanna. Selenium nanoparticles: A review on synthesis and biomedical applications. *Materials Advances*, **3**:1415–31, (2022).

[24] D. Serov, V. Khabatova, V. Vodeneev, R. Li, and S. Gudkov. A review of the antibacterial, fungicidal and antiviral properties of selenium nanoparticles. *Materials (Basel)*, **16**(15), (2023).

[25] C. Zhang, X. Zhai, G. Zhao, F. Ren, and X. Leng. Synthesis, characterization, and controlled release of selenium nanoparticles stabilized by chitosan of different molecular weights. *Carbohydrate Polymers*, **134**:158–66, (2015).

[26] M. S. Devi, S. Srinivasan, and A. Muthuvel. Selenium nanomaterial is a promising nanotechnology for biomedical and environmental remediation: A detailed review. *Biocatalysis and Agricultural Biotechnology*, **51**:102766, (2023).

[27] J. Zhang, X. Wang, and T. Xu. Elemental selenium at nano size (Nano-Se) as a potential chemopreventive agent with reduced risk of selenium toxicity: comparison with se-methylselenocysteine in mice. *Toxicological Sciences*, **101**:22–31, (2008).

[28] Z. J. Zhang JinSong, W. H. Wang HuaLi, B. Y. Bao YongPing, and Z. L. Zhang Lide. Nano red elemental selenium has no size effect in the induction of seleno-enzymes in both cultured cells and mice. , (2004).

[29] V. Nayak, K. R. Singh, A. K. Singh, and R. P. Singh. Potentialities of selenium nanoparticles in biomedical science. *New Journal of Chemistry*, **45**:2849–78, (2021).

[30] S. A. Wadhwani, U. U. Shedbalkar, R. Singh, and B. A. Chopade. Biogenic selenium nanoparticles: current status and future prospects. . *Applied Microbiology and Biotechnology*, **100**:2555–66, (2016).

[31] S. Chaudhary, A. Umar, and S. Mehta. Selenium nanomaterials: an overview of recent developments in synthesis, properties and potential applications. *Progress in Materials Science*, **83**:270–329, (2016).

[32] A. Khezri, A. Karimi, F. Yazdian, M. Jokar, S. R. Mofradnia, H. Rashedi, et al. Molecular dynamic of curcumin/chitosan interaction using a computational molecular approach: Emphasis on biofilm reduction. *International Journal of Biological Macromolecules*, **114**: 972–8, (2018).

[33] S. Zeng, Y. Ke, Y. Liu, Y. Shen, L. Zhang, C. Li, et al. Synthesis and antidiabetic properties of chitosan-stabilized selenium nanoparticles. *Colloids and Surfaces B: Biointerfaces*, **170**:115–21, (2018).

[34] A. Anitha, V. D. Rani, R. Krishna, V. Sreeja, N. Selvamurugan, S. Nair, et al. Synthesis, characterization, cytotoxicity and antibacterial studies of chitosan, O-carboxymethyl and N, O-carboxymethyl chitosan nanoparticles. *Carbohydrate Polymers*, **78**:672–7, (2009).

[35] Z. Shariatinia. Carboxymethyl chitosan: Properties and biomedical applications. . *International Journal of Biological Macromolecules*, **120**:1406–19, (2018).

[36] J. Song, C. Zhang, S. Kong, F. Liu, W. Hu, F. Su, et al. Novel chitosan based metal-organic polyhedrons/enzyme hybrid hydrogel with antibacterial activity to promote wound healing. *Carbohydrate Polymers*, :119522, (2022).

[37] N. Alizadeh and S. Malakzadeh. Antioxidant, antibacterial and anti-cancer activities of β-and γ-CDs/curcumin loaded in chitosan nanoparticles. *International Journal of Biological Macromolecules*, **147**:778–91, (2020).

[38] M. Darroudi, A. Rangrazi, K. Ghazvini, H. Bagheri, and A. Boruziniat. Antimicrobial activity of colloidal selenium nanoparticles in chitosan solution against Streptococcus mutans, Lactobacillus acidophilus, and Candida albicans. *Pesquisa Brasileira em Odontopediatria e Clínica Integrada*, **21**:e0121, (2021).

[39] Q. Yuan, R. Xiao, M. Afolabi, M. Bomma, and Z. Xiao. Evaluation of antibacterial activity of selenium nanoparticles against food-borne pathogens. *Microorganisms*, **11**:1519, (2023).

[40] A. Rangrazi, H. Bagheri, K. Ghazvini, A. Boruziniat, and M. Darroudi. Synthesis and antibacterial activity of colloidal selenium nanoparticles in chitosan solution: a new antibacterial agent. . *Materials Research Express*, **6**:1250h3, (2020).

[41] Q. Ruan, L. Yuan, S. Gao, X. Ji, W. Shao, J. Ma, et al. Development of ZnO/selenium nanoparticles embedded chitosan-based anti-bacterial wound dressing for potential healing ability and nursing care after paediatric fracture surgery. . *International Wound Journal*, **20**:1819–31, (2023).

[42] Y. Mori, T. Ono, Y. Miyahira, V. Q. Nguyen, T. Matsui, and M. Ishihara. Antiviral activity of silver nanoparticle/chitosan composites against H1N1 influenza A virus. *Nanoscale Research Letters*, **8**:1–6, (2013).

[43] Y. Li, Z. Lin, G. Gong, M. Guo, T. Xu, C. Wang, et al. Inhibition of H1N1 influenza virus-induced apoptosis by selenium nanoparticles functionalized with arbidol through ROS-mediated signaling pathways. *Journal of materials chemistry B*, **7**:4252–62, (2019).

[44] Y. Li, Z. Lin, M. Guo, Y. Xia, M. Zhao, C. Wang, et al. Inhibitory activity of selenium nanoparticles functionalized with oseltamivir on H1N1 influenza virus. *International Journal of Nanomedicine*, **12**: 5733, (2017).

[45] T. Xu, J. Lai, J. Su, D. Chen, M. Zhao, Y. Li, et al. Inhibition of H3N2 influenza virus induced apoptosis by selenium nanoparticles with chitosan through ROS-mediated signaling pathways. *ACS Omega*, **8**: 8473–80, (2023).

[46] S. C. Gupta, S. Patchva, and B. B. Aggarwal. Therapeutic roles of curcumin: lessons learned from clinical trials. . *The AAPS Journal*, **15**:195–218, (2013).

[47] N. Ghalandarlaki, A. M. Alizadeh, and S. Ashkani-Esfahani. Nanotechnology-applied curcumin for different diseases therapy. *BioMed Research International*, **2014**:394264, (2014).

[48] S. Hafez Ghoran, A. Calcaterra, M. Abbasi, F. Taktaz, K. Nieselt, and E. Babaei. Curcumin-based nanoformulations: A promising adjuvant towards cancer treatment. *Molecules*, **27**:5236, (2022).

[49] A. Anitha, S. Maya, N. Deepa, K. Chennazhi, S. Nair, and R. Jayakumar. Curcumin-loaded N,O-carboxymethyl chitosan nanoparticles for cancer drug delivery. *Journal of Biomaterials Science, Polymer Edition*, **23**:1381–400, (2012).

[50] V. Mikušová and P. Mikuš. Advances in chitosan-based nanoparticles for drug delivery. *International Journal of Molecular Sciences*, **22**: 9652, (2021).

[51] W. Chen, Y. Li, S. Yang, L. Yue, Q. Jiang, and W. Xia. Synthesis and antioxidant properties of chitosan and carboxymethyl chitosan-stabilized selenium nanoparticles. *Carbohydrate Polymers*, **132**: 574–81, (2015).

[52] J. O. Akolade, H. O. B. Oloyede, M. O. Salawu, A. O. Amuzat, A. I. Ganiyu, and P. C. Onyenekwe. Influence of formulation parameters on encapsulation and release characteristics of curcumin loaded in chitosan-based drug delivery carriers. *Journal of Drug Delivery Science and Technology*, **45**:9–11, (2018).

[53] R. S. Nair, A. Morris, N. Billa, and C.-O. Leong. An evaluation of curcumin-encapsulated chitosan nanoparticles for transdermal delivery. *Aaps Pharmscitech*, **20**:69, (2019).

[54] D. D. Lee, E. Y. Lee, S. H. Jeong, and C. L. Chang. Evaluation of a colorimetric broth microdilution method for antimicrobial susceptibility testing using 2, 3, 5-triphenyltetrazolium chloride. *Korean J Clin Microbiol.*, **10**:49–53, (2007).

[55] S. Boroumand, M. Safari, E. Shaabani, M. Shirzad, and R. Faridi-Majidi. Selenium nanoparticles: synthesis, characterization and study of their cytotoxicity, antioxidant and antibacterial activity. . *Materials Research Express*, **6**:0850d8, (2019).

[56] A. Abdoli, R. Aalizadeh, H. Aminianfar, Z. Kianmehr, A. Teimoori, E. Azimi, et al. Safety and potency of BIV1-CovIran inactivated vaccine candidate for SARS-CoV-2: A preclinical study. . *Reviews in medical virology*, 32:e2305, (2022).

[57] M. Salehi, H. Hosseini, H. R. Jamshidi, H. Jalili, P. Tabarsi, M. Mohraz, et al. Assessment of BIV1-CovIran inactivated vaccine–elicited neutralizing antibody against the emerging SARS-CoV-2 variants of concern. *Clinical Microbiology and Infection*, **28**:e1–e7, (2022).

[58] D. A. Serov, V. V. Khabatova, V. Vodeneev, R. Li, and S. V. Gudkov. A review of the antibacterial, fungicidal and antiviral properties of selenium nanoparticles. *Materials*, **16**:5363, (2023).

[59] Z.-H. Lin and C. C. Wang. Evidence on the size-dependent absorption spectral evolution of selenium nanoparticles. *Materials Chemistry and Physics*, **92**:591–4, (2005).

[60] C. An, K. Tang, X. Liu, and Y. Qian. Large-scale synthesis of high quality trigonal selenium nanowires. *European Journal of Inorganic Chemistry*, **2003**:3250–5, (2003).

[61] A. Sentkowska and K. Pyrzyńska. The influence of synthesis conditions on the antioxidant activity of selenium nanoparticles. *Molecules*, **27**:2486, (2022).

[62] G. Suriati, M. Mariatti, and A. Azizan. Synthesis of silver nanoparticles by chemical reduction method: Effect of reducing agent and surfactant concentration. *International Journal of Automotive and Mechanical Engineering*, **10**:1920–7, (2014).

[63] S. Das, K. Bandyopadhyay, and M. Ghosh. Effect of stabilizer concentration on the size of silver nanoparticles synthesized through chemical route. *Inorganic Chemistry Communications*, **123**:108319, (2021).

[64] A. Tsuboi, K. Nakamura, and N. Kobayashi. Multicolor electrochromism showing three primary color states (cyan–magenta–yellow) based on size-and shape-controlled silver nanoparticles. *Chemistry of Materials*, **26**:6477–85, (2014).

[65] L. Liu, Z. Xiao, S. Niu, Y. He, G. Wang, and X. Pei. Preparation, characteristics and feeble induced-apoptosis performance of non-dialysis requiring selenium nanoparticles@ chitosan. . *Materials & Design*, **182**:108024, (2019).

[66] Y. Chen, S. Stoll, H. Sun, X. Liu, W. Liu, and X. Leng. Stability and surface properties of selenium nanoparticles coated with chitosan and sodium carboxymethyl cellulose. . *Carbohydrate Polymers*, **278**: 118859, (2022).

[67] S. S. Salem. Bio-fabrication of selenium nanoparticles using Baker's yeast extract and its antimicrobial efficacy on food borne pathogens. *Applied Biochemistry and Biotechnology*, **194**:1898–910, (2022).

[68] L. Patle, P. Labhane, V. Huse, K. Gaikwad, and A. Chaudhari. Synthesis and structural analysis of Fe doped TiO_2 nanoparticles using Williamson Hall and Scherer Model. *AIP Conference Proceedings*, , (2018).

[69] S.-Y. Zhang, J. Zhang, H.-Y. Wang, and H.-Y. Chen. Synthesis of selenium nanoparticles in the presence of polysaccharides. *Materials Letters*, **58**:2590–4, (2004).

[70] S. Mustapha, J. Tijani, M. Ndamitso, A. Abdulkareem, D. Shuaib, A. Amigun, et al. Facile synthesis and characterization of TiO_2 nanoparticles: X-ray peak profile analysis using Williamson–Hall and Debye–Scherrer methods. *International Nano Letters*, **11**:241–61, (2021).

[71] S. Mustapha, M. Ndamitso, A. Abdulkareem, J. Tijani, D. Shuaib, A. Mohammed, et al. Comparative study of crystallite size using Williamson-Hall and Debye-Scherrer plots for ZnO nanoparticles. *Advances in Natural Sciences: Nanoscience and Nanotechnology*, **10**:045013, (2019).

[72] S. G. Pandya, J. P. Corbett, W. M. Jadwisienczak, and M. E. Kordesch. Structural characterization and X-ray analysis by Williamson–Hall method for Erbium doped Aluminum Nitride nanoparticles, synthesized using inert gas condensation technique. *Physica E: Low-dimensional Systems and Nanostructures*, **79**:98–102, (2016).

[73] M. A. Ruiz-Fresneda, S. Schaefer, R. Hübner, K. Fahmy, and M. L. Merroun. Exploring antibacterial activity and bacterial-mediated allotropic transition of differentially coated selenium nanoparticles. *ACS Applied Materials & Interfaces*, **15**:29958–70, (2023).

[74] N. A. Rosli, Y. H. Teow, and E. Mahmoudi. Current approaches for the exploration of antimicrobial activities of nanoparticles. *Science and Technology of Advanced Materials*, **22**:885–907, (2021).

[75] J. Muchová, V. Hearnden, L. Michlovská, L. Vištejnová, A. Zavadáková, K. Šmerková, et al. Mutual influence of selenium nanoparticles and FGF2-STAB® on biocompatible properties of collagen/chitosan 3D scaffolds: *In vitro* and ex ovo evaluation. . *Journal of Nanobiotechnology*, **19**:1–16, (2021).

[76] J. Dorazilová, J. Muchová, K. Šmerková, S. Kočiová, P. Diviš, P. Kopel, et al. Synergistic effect of chitosan and selenium nanoparticles on biodegradation and antibacterial properties of collagenous scaffolds designed for infected burn wounds. . *Nanomaterials*, **10**: 1971, (2020).

[77] T. Abou Elmaaty, K. Sayed-Ahmed, H. Elsisi, S. M Ramadan, H. Sorour, M. Magdi, et al. Novel antiviral and antibacterial durable polyester fabrics printed with selenium nanoparticles (SeNPs). *Polymers*, **14**:955, (2022).

[78] T. Abou Elmaaty, K. Sayed-Ahmed, R. Mohamed Ali, K. El-Khodary, and S. A. Abdeldayem. Simultaneous sonochemical coloration and antibacterial functionalization of leather with selenium nanoparticles (SeNPs). *Polymers*, **14**:74, (2021).

[79] L. Mao, L. Wang, M. Zhang, M. W. Ullah, L. Liu, W. Zhao, et al. In situ synthesized selenium nanoparticles-decorated bacterial cellulose/gelatin hydrogel with enhanced antibacterial, antioxidant, and anti-inflammatory capabilities for facilitating skin wound healing. *Advanced Healthcare Materials*, **10**:2100402, (2021).

[80] H. E. Touliabah, M. M. El-Sheekh, and M. E. M. Makhlof. Evaluation of Polycladia myrica mediated selenium nanoparticles (PoSeNPS) cytotoxicity against PC-3 cells and antiviral activity against HAV HM175 (Hepatitis A), HSV-2 (Herpes simplex II), and Adenovirus strain 2. *Frontiers in Marine Science*, **9**:1092343, (2022).

[81] J. Zhong, Y. Xia, L. Hua, X. Liu, M. Xiao, T. Xu, et al. Functionalized selenium nanoparticles enhance the anti-EV71 activity of oseltamivir in human astrocytoma cell model. *Artificial Cells, Nanomedicine, and Biotechnology*, **47**:3485–91, (2019).

[82] M. Cotten and M. V. Phan. Evolution of increased positive charge on the SARS-CoV-2 spike protein may be adaptation to human transmission. *Iscience*, **26**(3), (2023).